

## Cellular structures in three-dimensional directional solidification: Simulation and analysis

K. Kassner,<sup>1</sup> J.-M. Debierre,<sup>2</sup> B. Billia,<sup>2</sup> N. Noël,<sup>2</sup> and H. Jamgotchian<sup>2</sup>

<sup>1</sup>*Institut für Theoretische Physik, Otto-von-Guericke-Universität Magdeburg, Postfach 4120, D-39016 Magdeburg, Germany*

<sup>2</sup>*Laboratoire MATOP, Associé au CNRS, Faculté des Sciences de St. Jérôme, Case 151, 13397 Marseille Cedex 20, France*

(Received 28 April 1997; revised manuscript received 17 October 1997)

The use of an asymptotically valid interface equation for directional solidification allows numerical studies of the evolution of three-dimensional cellular structures in extended systems. We consider systems that are large enough to render a statistical description of disordered structures meaningful and to enable a direct comparison with experiment. Moreover, it is possible to assess the stability of the observed patterns on the basis of long-time simulations. In addition to statistical methods already employed in the analysis of experiments, new statistical tools are introduced to follow the dynamics of the system. In general, three growth phases can be distinguished. During the first, short one, the pattern dynamically selects its preferred length scale by a coarsening or a fine-graining process. In the second, much longer phase, the cells rearrange, evolving towards a polycrystalline, essentially ordered structure. In the third phase, a process of gradual elimination of defects takes place. For smaller temperature gradients, there is an evolution towards oscillating patterns. Oscillations lead to a reduction of the percentage of defects, unless they act as a precursor to weak turbulence, which happens at even lower values of the temperature gradient. [S1063-651X(98)00703-X]

PACS number(s): 64.70.Dv, 81.30.Fb

### I. INTRODUCTION

Directional solidification has become a paradigmatic experiment for the investigation of pattern formation at interfaces between two phases that transform into each other via a first-order phase transition. This includes ordinary solidification [1,2], but also various liquid-crystal transitions [3,4].

Many experiments have focused on thin samples, trying to realize an essentially two-dimensional setup [5–9], which is more amenable to theoretical analysis than a three-dimensional system. Indeed, the theory of two-dimensional solidification has been developed quite far [10–28] and successfully explained a plethora of observations.

Experiments on samples extending in all three dimensions posed certain difficulties regarding their dynamical interpretation because direct observation was not possible [29,30]. Transverse cuts had to be made and treated by etching to gain access to the cellular structure. By using transparent materials and carefully planned optical arrangements, it recently has become feasible to continually monitor the growth of massive samples and to follow the dynamical evolution *in situ* [31].

Theoretical approaches have also concentrated on the two-dimensional case [32] for a variety of reasons. First, it is more easily treated both analytically and numerically. Second, sophisticated Green's-function methods of solving the model equations [33] become inefficient in three dimensions. Third, it is a formidable task to track the interface between the liquid and solid phases in three-dimensional systems [34]. The last problem is avoided in *phase-field models*, and there have been numerical simulations based on this approach, dealing with free growth of single dendrites [35–37] or fingerlike structures [38] and with directional solidification of a few (on the order of 10) cells [39]. Large-scale simulations of samples containing several hundreds of cells, however, are still beyond the scope of these methods.

Therefore, we have chosen a different approach in the present paper. We start from a partial differential equation for the two-dimensional *interface* between the liquid and solid phases. This equation was derived as a description of rapid solidification and is asymptotically valid near the absolute stability limit [28,40,41].

Since the experiments we wish to discuss are done at moderate pulling velocities, we do not expect more than qualitative agreement with our simulations. On the other hand, we are confident about the generic character of our results on cellular growth. Comparisons with another, more generic interface equation, the damped Kuramoto-Sivashinsky equation, have shown that secondary instabilities are the same for the two equations, in both one [42] and two dimensions [43,44]. Moreover, it will emerge from this paper that a reasonable description of experimental cellular structures is feasible on the basis of our equation. We can easily simulate some 2000 cells, which has been shown to be more than sufficient [45] for a statistical description of the results.

Section II of the paper gives our basic interface equation and some comments on the numerical implementation. In Sec. III we discuss the statistical quantities considered in our simulations and how to measure them. Section IV describes a series of numerical results for a variety of temperature gradients and discusses the long-time dynamics. We compare the statistics of minimum spanning trees on these structures with similar quantities calculated for experimental patterns. In Sec. V the results are discussed and some conclusions are drawn.

### II. MODEL

Our computations will be based on the following equation, derived from a Sivashinsky-type singular expansion about the point of absolute stability [28]:

$$\begin{aligned}
\zeta_{tt} - \left(2 + \frac{1}{k} + \nu\right) \nabla^2 \zeta_t + \left(1 + \frac{1}{k} + \nu^2\right) \nabla^4 \zeta + 8k \nabla^2 \zeta + 8k \bar{G} \zeta \\
= 2 \zeta_t \nabla^2 \zeta + 2(|\nabla \zeta|^2)_t - 2 \nabla^2(|\nabla \zeta|^2) - 2\nu(\nabla \zeta) \nabla(\nabla^2 \zeta) \\
- \frac{2}{k} \nabla[(\nabla \zeta) \nabla^2 \zeta] - 2 \nabla[(\nabla \zeta) |\nabla \zeta|^2].
\end{aligned}$$

Herein the gradient operator is two dimensional,  $\nabla = (\partial_x, \partial_y)$ , and  $\zeta(x, y, t)$  is the height of the liquid-solid interface; the temperature gradient is oriented along the  $z$  axis.

There are three nondimensional parameters in the equation: the segregation coefficient  $k$ , the ratio  $\nu = D_s/D$  of the diffusion coefficients for impurities in the solid and the liquid, and the nondimensional temperature gradient  $\bar{G}$ . Solute trapping is neglected. The *one-sided model* is characterized by  $\nu=0$ , the *symmetric model* by  $\nu=1$ .  $\bar{G}$  is related to physical parameters via

$$\bar{G} = \frac{8D^3 L^2 m \Delta c}{\gamma^2 T_m^2} \frac{G}{V(V_a - V)^2}. \quad (1)$$

In this expression,  $L$  is the latent heat (per unit volume) of the transition,  $m$  is the absolute value of the slope of the liquidus line,  $\Delta c$  is the miscibility gap at the base temperature  $T_0$  ( $T_0 = T_m - mc$ , with  $T_m$  the melting temperature of the pure substance),  $\gamma$  is the surface energy, assumed isotropic here,  $V_a$  is the velocity corresponding to the absolute stability limit, given by  $V_a = mL\Delta cD/\gamma T_m k$ ,  $G$  is the temperature gradient, and  $V$  is the pulling velocity.

Note that Eq. (1) becomes indefinite for  $k=0$  because there is no absolute stability limit in this case. For simplicity, we shall set  $k=1$  in the following, i.e.,  $\Delta c = \text{const}$ . We do not expect this choice to have a strong influence on the results.

Moreover, most of the detailed results presented here were obtained within the *symmetric* model, which is not a realistic model for directional solidification (as opposed to directional ordering in liquid crystals), but is least problematic in numerical simulations since it is not very susceptible to the accidental evolution of deep grooves that can easily trigger numerical instabilities. Experience from previous simulations of one-dimensional interfaces [28] suggests that the generic patterns are independent of the ratio of diffusion constants.

Equation (1) was implemented on both square and hexagonal numerical grids using second-order accurate direct schemes of discretization and constant time steps in the temporal integration. More sophisticated implementations may become necessary in going to extremely long times, but with the present scheme we could simulate systems containing on the order of 2000 solidification cells for as long as 30 000 diffusion times [46], which seems sufficient to compare with experiments. There are certain theoretical questions, discussed in Sec. IV, whose answers might require even longer simulations.

Boundary conditions were usually periodic, and a hexagonal geometry (with underlying hexagonal grid) was also considered to make sure that the overall results were not an

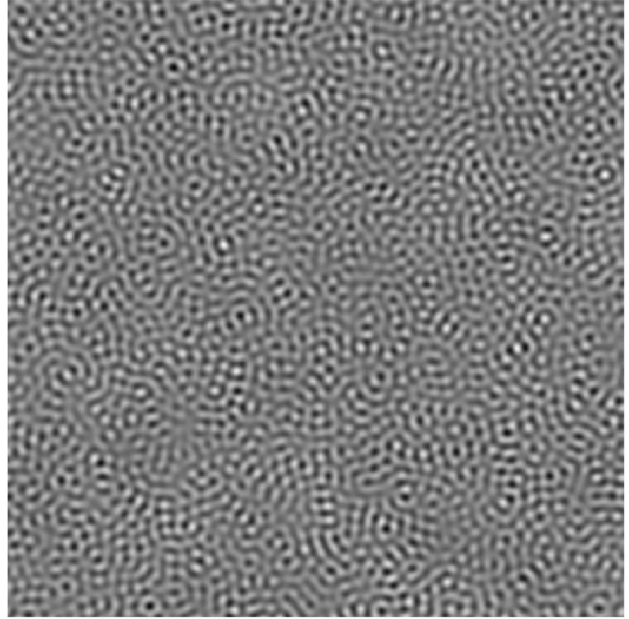


FIG. 1. Simulated surface of solidification pattern,  $t=10$  diffusion times after initialization with random interface.  $\bar{G}=0.6$ ,  $k=1$ , and  $\nu=1$ . The system size in diffusion lengths is  $256 \times 256$ . Gray-scale code: Lighter pixels correspond to more elevated interface points, darker ones to lower-lying points.

artifact of our restricting hexagonal cell structures to a rectangular (albeit very large) periodicity unit. Results similar to the ones that are reported here have been obtained with reflecting and helical boundary conditions.

### III. STATISTICAL ANALYSIS

#### A. Cluster number function

Figure 1 shows a typical interface, initiated with random noise, after ten diffusion times. A cellular structure has not yet fully developed, but a dominant length scale is clearly visible.

An approach to analyzing solidification interfaces, developed by Billia *et al.* [45], is based on image processing of a digitized picture of the interface. Introducing a threshold gray level and changing into black each pixel that is darker and into white each one that is lighter, they obtain a binary image, an example of which is given in Fig. 2. White areas correspond to solidification cells, black ones to the grooves in between. This binary image can then be analyzed via the construction of the centers of mass of the cells and the minimum spanning tree of the centers. The cell shapes may be approximated by a weighted Wigner-Seitz or rather Voronoi construction [45]. While this approach is a valuable starting point for what we shall present here, it is obviously restricted to a situation where a clearly distinguishable cellular structure is present. This is not yet the case in Fig. 1.

A more complete characterization that also takes into account some of the interface extension into the third dimension (the  $z$  direction) and allows one to construct the minimum spanning tree from the numeric representation of the interface without the need of an intermediate image processing step is based on the following ideas. We introduce a

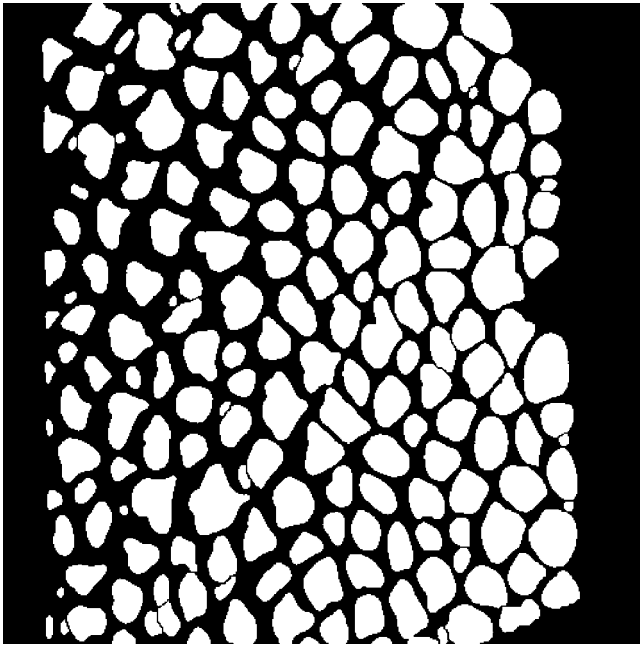


FIG. 2. Binary picture of solidification cells from an experiment with succinonitrile 0.5 wt. acetone ( $V=2.1 \mu\text{m/s}$ ).

number of equidistant height levels of the interface, which may be thought of as representing the grey levels in an image. At each of these levels we cut the interface by a horizontal plane  $z=z_0=\text{const}$ . Each interface point (on the numerical grid) that is above the cut (i.e., for which  $z>z_0$ ) will be counted as *particle within a cluster*. In a digitized image, each such point would correspond to a (white) pixel. For each cut, the number  $N(z_0)$  of different clusters is determined. We call  $N(z)$  the cluster number function and an example, corresponding to the interface of Fig. 1, is given in Fig. 3. Obviously, this function itself is a means of characterizing the shape of the interface via the topology of cuts

through it. Thus its temporal evolution may yield information about the dynamics of a disordered system. Also, it may be used to effect the construction of a minimum spanning tree, which in the case of cellular structures will essentially coincide with the one obtained from image processing, but allows the *definition* of a minimum spanning tree for more general situations.

This is achieved as follows. For any disordered structure the cluster number function will exhibit a well-defined maximum. At small threshold levels there is just one cluster because the whole mountainous landscape above the threshold remains connected. At large thresholds only the tip of the highest mountain surpasses the threshold, therefore there is also just one cluster. In between, the function, assuming it varies in a continuous manner, must have at least one maximum, and usually there is just a single one (see Fig. 3). The threshold corresponding to this maximum will lead to a binary image containing the largest possible number of substructures, so it is natural to identify the clusters at this threshold with solidification cells. As it turns out, this approach works well at least for the construction of the minimum spanning tree and the determination of its statistical properties. In order to extract cell shapes, one would presumably wish (this is suggested by a comparison of the binary images obtained with this method and those produced “by hand” in the analysis of experimental pictures) to take a somewhat smaller value of the threshold. So one will lose some cells by not resolving certain pairs of closely spaced cells, but get a better overall approximation for the shape of the remaining ones. However, we will not concern ourselves with cell shapes here.

Recently, an approach to the morphological characterization of patterns has been suggested by Mecke that bears some similarities to the one chosen here [47]. In particular, Mecke points out that autocorrelation functions and spatial Fourier transforms, while providing useful information about characteristic length scales, cannot distinguish well between

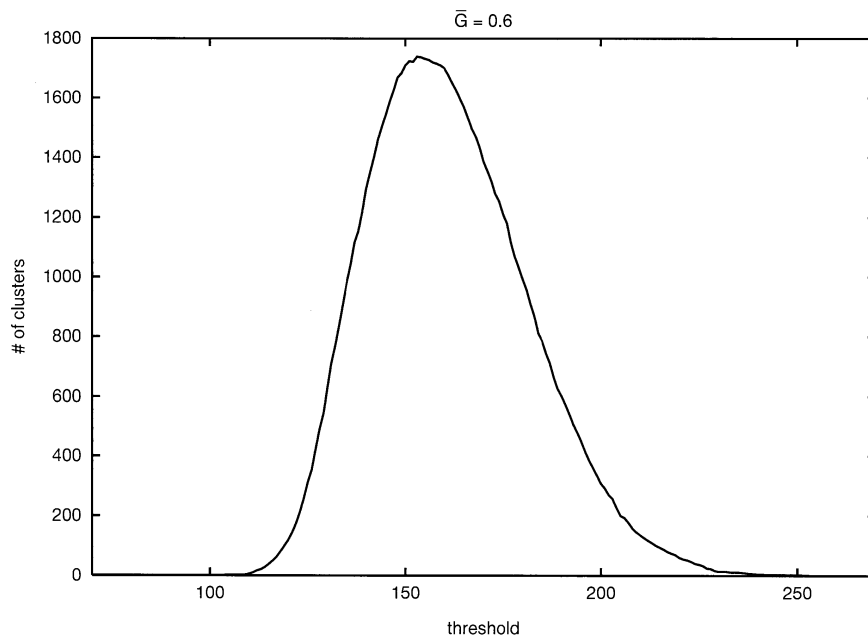


FIG. 3. Cluster number function for  $\bar{G}=0.6$  and  $t=10.0$ .

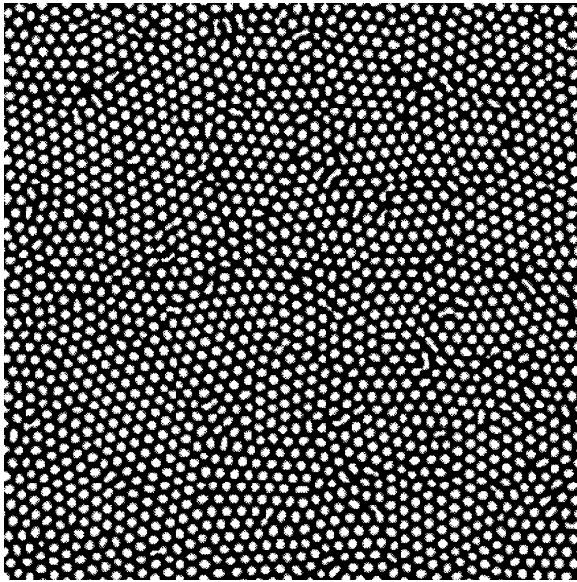


FIG. 4. Binary picture of cell structure for  $\bar{G}=0.6$ .

irregular structures with the same length scales. He then proposes to use certain Minkowski functionals as *morphological* measures for patterns, quantities that are well known in image analysis, mathematical morphology [48], and integral geometry [49]. Their definition is based, as that of the cluster number function, on cutting the interface by a series of equidistant levels or, alternatively, dividing its gray-scale image into a number, usually 256, of gray levels (supposedly corresponding to the interface levels) and setting the gray value of each pixel to 0 or 1, depending on whether or not it exceeds a threshold value. This produces 256 black-and-white pictures out of a single gray-level one and yields, for each level ( $z_0$ ), the so-called level contours, which in the language used here are just the contours of the clusters. Among the measures considered in [47] is the Euler characteristic  $\chi$ , a topological quantity. It is related to our cluster number function because it is essentially the difference between the numbers of white and black clusters. Its calculation, however, is simpler than that of the cluster number function because it can be done *locally*, without explicit counting of the clusters [47]. Nevertheless, since the calculation of the latter takes a very small percentage of the total computation time, we did not change conventions after learning about the approach of [47]. Moreover, it seems to us that the cluster number function is conceptually somewhat simpler than the Euler characteristics.

### B. Minimum spanning tree

Figure 4 exhibits an example for the binary image of a computed structure and Fig. 5 that of the corresponding minimum spanning tree, both obtained with a threshold value 10% smaller than that corresponding to the maximum of the cluster number function. This picture is to be compared with Fig. 2, an image obtained from an experimental structure by a judicious choice of the threshold value while doing interactive image processing. While cellular shapes are somewhat better represented in this picture than in one obtained with the “schematic” choice of the threshold *at* the maximum of the cluster number function, the latter choice (not shown)

$$\bar{G} = 0.6, t = 100.0$$

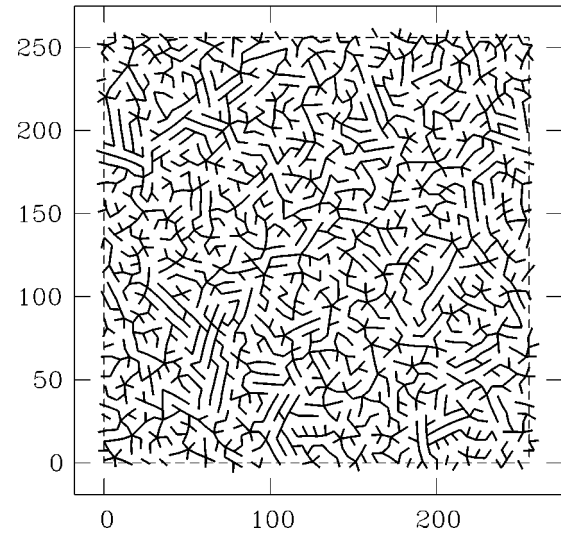


FIG. 5. Minimum spanning tree corresponding to the binary picture of Fig. 4.

turns out to be sufficient for a construction of the cell centers and the minimum spanning tree.

It may be pointed out that we can now associate a minimum spanning tree with *any* pattern, be it cellular or not. For our present purposes, however, it is sufficient to use the prescription outlined above, *viz.*, to obtain well-defined cells by choosing the threshold at the maximum of the cluster number function. In the analysis of experiments, one usually takes out the cells at the boundary of the digitized image in order not to bias the statistics, as peripheral cells are incomplete and their centers of mass do not correspond to the true center of the completed cell [45]. For the numerics with periodic boundary conditions, it is more appropriate to construct the periodically continued tree. So we take into account periodic image points in calculating distances between cell centers. This is why there are branches of the tree that “cross the border” of the picture and may make it appear disconnected, although it is not. Recall that it is defined on a torus topology, imposed by the periodic boundary conditions.

The simplest pieces of quantitative information that can be extracted from the tree are the aforementioned average length of its edges and their standard deviation. Normalizing both quantities by division by the square root of the average cell area and calling the normalized versions  $m$  and  $\sigma$ , respectively, we obtain a point in the  $m\sigma$  diagram, originally introduced by Dussert *et al.* [50]. The temporal evolution of this point in the plane spanned by  $m$  and  $\sigma$  has been used by Billia *et al.* [45] to characterize experimental structures and we will do the same with simulated structures.

It should be noted that the edges of the minimum spanning tree form a subset of the edges in a full graph of all nearest-neighbor pairs obtained via the Voronoi construction. Evidently, this subset exhibits a preference of short distances over long ones. Thus an overall increase of the average is not to be interpreted, even at constant cell number, as an increase in the average distance of the cells; it might as well mean that the distances become less widely distributed.

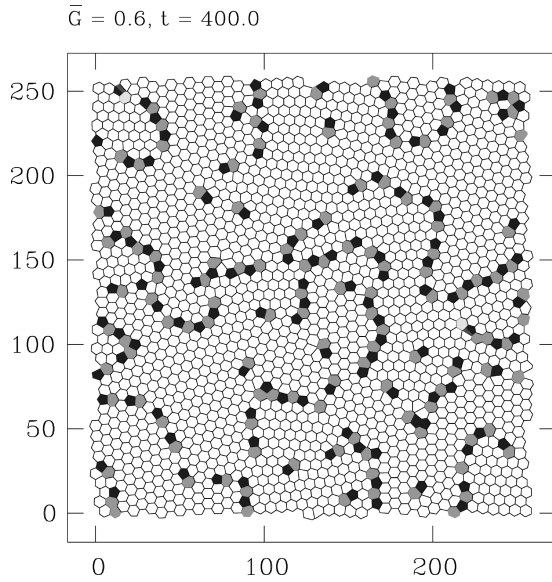


FIG. 6. Voronoi diagram of a solidification pattern for  $\bar{G}=0.6$  at  $t=400$  (continuing the evolution of Fig. 1). Pentagons are shaded dark and heptagons light gray.

### C. Defects

For long simulation times, neither the minimum spanning tree nor the cluster number function exhibits strong changes anymore. A useful means of characterization in this regime is the number of defects in the pattern. Their definition is based on the Voronoi diagram of the cell centers. Each cell that has a number of neighbors different from six is considered a defect. Figure 6 gives an example of the Voronoi cells of a system at an intermediate time ( $t=400$ ); defect cells are shaded, hexagonal cells remain white.

Even in this example of very moderate time we see the two basic tendencies: defects tend to assemble in lines, *dynamic grain boundaries*, and (except at very early times) they come almost exclusively in pairs of pentagons and heptagons, very similar to the situation encountered in experiments on Bénard-Marangoni convection [51]. We will discuss the temporal evolution of defect numbers in the next section. Similar defect counting ideas have been employed before in the discussion of the topology of two-dimensional soap froths [52].

## IV. SIMULATION RESULTS

From linear stability analysis it is known that a planar interface becomes unstable for values of  $\bar{G}$  below [28]

$$\bar{G}_c = \frac{2k^2}{1+k+k\nu^2}, \quad (2)$$

i.e., for the symmetric model with  $k=1$ , the critical temperature gradient is  $\frac{2}{3}$ . This suggests to investigate systems both in the vicinity and far from this value. In particular, we report here on the long-time dynamics of systems with values of  $\bar{G}$  between 0.35 and the critical value. Time is always measured in units of the diffusion time.

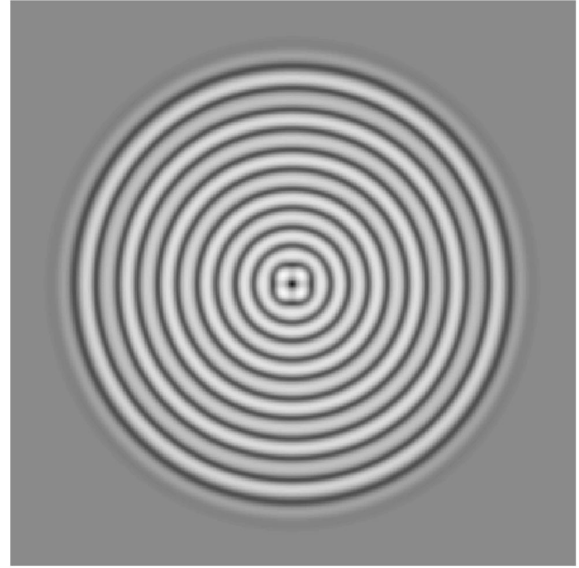


FIG. 7. Pattern obtained from a nucleus without initial noise.  $\bar{G}=0.35, t=40$ , and the system size is  $179.2 \times 179.2$ .

### A. Early dynamics

In most cases, we took a random interface as initial condition. Figure 1 shows a very early stage of the system with  $\bar{G}=0.6$ , which is 10% from the primary instability threshold towards the unstable side. The image definitely conveys the impression of a perturbed water surface.

This impression gets enhanced by a look at Fig. 7, a simulation starting from a circular Gauss-shaped nucleus ( $\bar{G}=0.35$  here). Apart from the center of the picture, where four almost square-shaped cells can be distinguished, this looks very much like the spreading of a water wave after a stone has been thrown in a pond. The picture was taken at  $t=40.0$  and the wave has almost reached the system boundaries, i.e., it has spread about 80 diffusion lengths in each direction, which yields an estimate of 2 for the wave speed. The pattern is circular, due to the fact that we used isotropic surface tension in the model equations.

When the wave reaches the system boundary, it starts to interfere with its periodic images and a cellular structure begins to develop, which at first maintains the fourfold symmetry of the numerical box (and grid). Eventually, this symmetry gets broken by numerical noise, and after about 500 diffusion times, the statistical properties of structures from this run and one with random initial conditions were essentially the same, although remnants of the overall symmetry in the “nucleated” system were still perceptible.

Another type of initial condition used was a pattern with an imposed wavelength that was larger than the expected final value, in order to verify that the selected wavelength is also reached by a fine-graining procedure. The starting pattern was obtained from random initial conditions by waiting until the system had found its preferred wavelength and then multiplying the system size by some appropriate factor without changing any other parameter, to obtain a coarser structure. Again, the final system characteristics did not depend on the initial condition.

We will from now on focus on the “generic” random initial conditions. Let us note that *experimental* patterns at

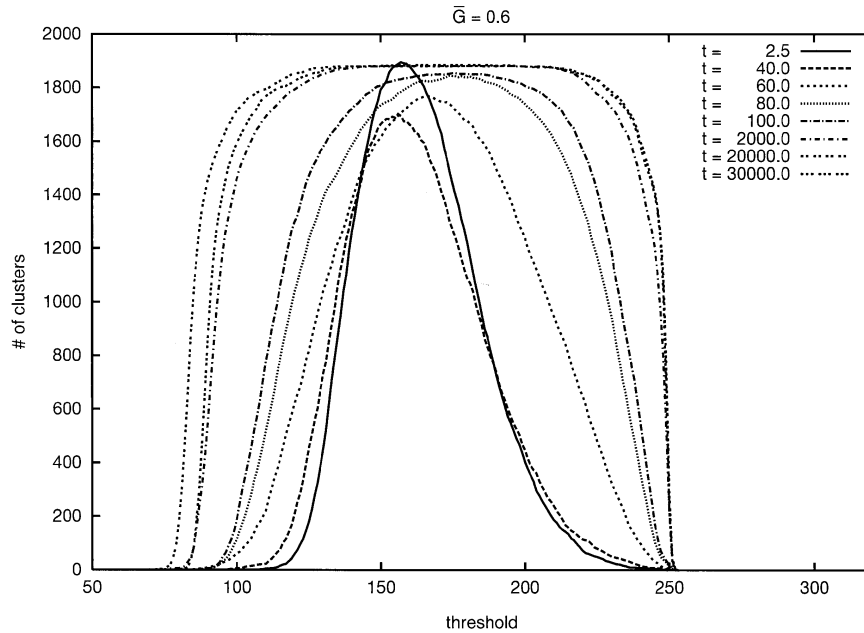


FIG. 8. Temporal evolution of the cluster number function for  $\bar{G}=0.6$  up to  $t=30\,000$ .

the beginning of solidification bear a strong similarity to Fig. 1.

With random initial conditions, the early stage of growth is best characterized using the cluster number function. In Fig. 8 we visualize its evolution by plotting it at several points in time chosen to render the different growth phases visible. Intermediate curves have been omitted in order not to overcrowd the picture.

Conspicuously, the initial change of the function (up to  $t=40$ ) mostly consists in a reduction of its height, whereas its shape remains essentially unchanged. This means that the relative distribution of cell heights does not change (note that cell heights are always mapped to an interval from 1 to 254, so absolute heights may, and do, change during this growth phase). However, the maximum of the cluster number function and hence the number of cells decrease. Thus the average size of cells increases and so does the dominant length scale of the pattern. A coarsening process is operative, resulting in the selection of a preferred length scale. This selection process is *local* because it is essentially finished before information can travel by diffusion across the entire system. Of course, its duration depends on the amplitude of the initial noise to some extent, but since growth is exponential initially, this dependence is slight for any reasonable level of noise (e.g., a few percent of the final cell size).

If we start from a too coarse structure instead of a too fine one, the time scale for length selection via cell splitting is somewhat larger. On choosing an extremely large initial wavelength (say, half the system size), we have to wait much longer to see the characteristic wavelength appear. In this case, the interface is smooth on small scales and the division into cells has to be triggered by numerical noise, which can take on the order of 1000 diffusion times.

### B. Intermediate stage

As demonstrated in Fig. 8, the second stage of growth is characterized by a drastically different behavior of the cluster

number function. Its *shape* now changes strongly whereas its *height* remains almost constant. A plateau develops around the maximum and the function seems to approach a rectangular shape.

To clarify what this means, we give a pattern in Fig. 9 that is completely ordered by construction (the profile is given by the analytic expression  $z(x,y)=\sin(qy)\cos[\frac{1}{2}(\sqrt{3}qx+qy-\pi/2)]\cos[\frac{1}{2}(\sqrt{3}qx-qy+\pi/2)]$ ) together with its cluster number function. A rectangular cluster number function corresponds to a structure consisting of cells where all bottoms and all tops of the cells are at the same heights, respectively. This situation strongly suggests a perfect underlying lattice.

Of course, given such a shape of the cluster number function, we cannot rigorously conclude a perfect lattice. The whole point of its introduction is a *reduction* of the *information* encoded in a complex interface structure to an easily digestible form. Therefore, one could artificially construct different interfaces with the same cluster number function. Hence it is important to look at more than a single measure for the topological properties of the interface. Incidentally, the cluster number function is one of the rare examples where the intuitive notion of increasing order being connected with a peak getting sharper fails: The opposite happens, as the peak is getting “smeared out” with increasing order.

As the plateau of the cluster number function widens, more and more cells acquire similar heights and it is natural to presume that this is due to the pattern becoming more ordered. This assumption may be confirmed by looking at the surface itself, given for  $t=100$  in Fig. 10 and for  $t=3300$  in Fig. 11. It is obvious that a well-developed cellular structure is already present in the first of these pictures and that the basic pattern corresponds to hexagonal order.

More precise statements on the degree of order attained are possible via construction of the minimum spanning tree, a *metrical* rather than *topological* measure, and by studying

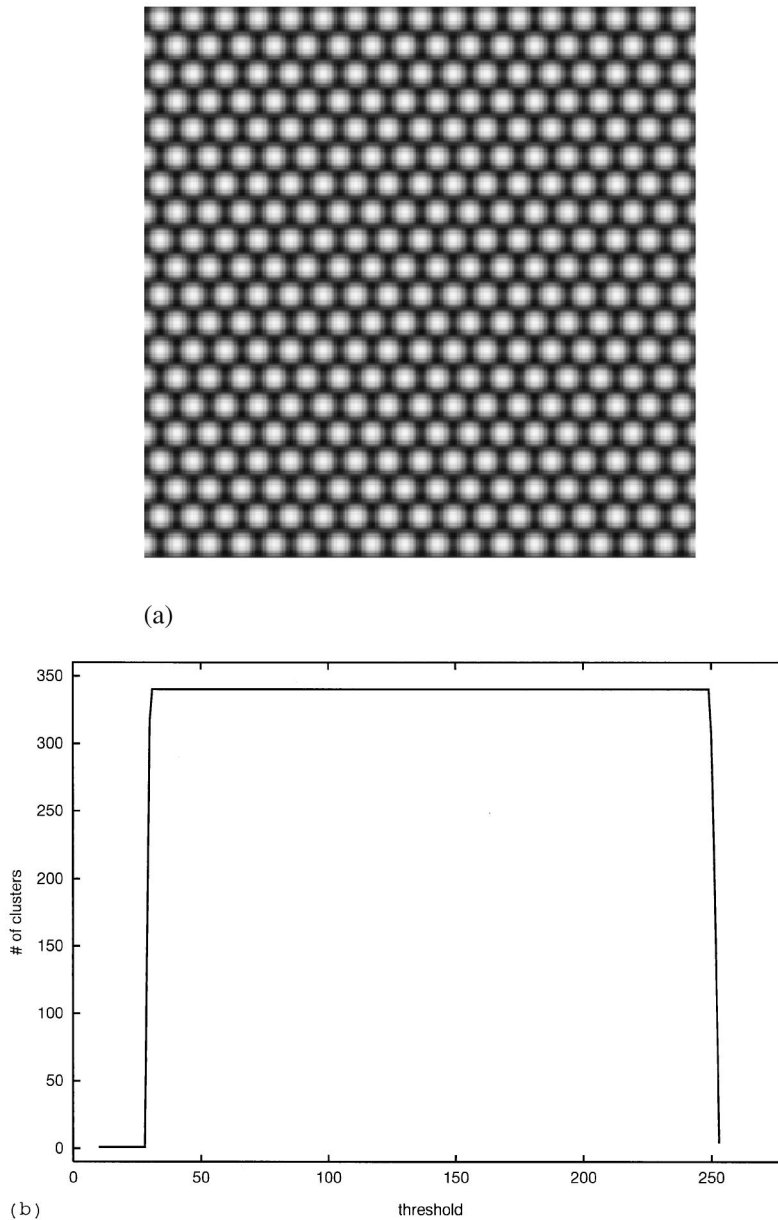


FIG. 9. Perfectly ordered structure (top) and its cluster number function (bottom).

the evolution of the number of defects of the pattern in the course of time. Comparing the minimum spanning tree corresponding to Fig. 10 with that corresponding to Fig. 11, we see that the tree clearly gives an impression of the polycrystalline structure of the pattern and, in particular, of the higher degree of order present in the second case (see Figs. 5 and 12). To make this statement more quantitative, we give Fig. 13 showing the  $m\sigma$  diagram for the temporal evolution of three systems for large time intervals.

This evolution was calculated from a sequence of interfaces obtained in the simulation. The dashed lines are best explained by looking at Fig. 14, displaying representative points for a variety of experimental and theoretical structures. Perfect lattices evidently must have standard deviation  $\sigma=0$  and as a consequence of the normalization via the cell areas a square lattice has  $m=1$ , while for a hexagonal lattice  $m=\sqrt{2/\sqrt{3}}\approx 1.075$ . The triangles correspond to some quasi-

periodic tilings, the squares to experimental points.

If the vertex positions of the hexagonal lattice are perturbed with Gaussian noise of increasing strength, the representative point of this lattice moves up along the curve in Fig. 14 connecting the hexagonal structure with a completely random distribution. The upper dashed line in Fig. 13 corresponds to this curve and its importance derives from the fact that experimental points seem to cluster near this line, meaning that the corresponding pattern may be considered a perturbed hexagonal structure. The lower dashed line of Fig. 13 represents a perturbed square pattern, also shown in Fig. 14. These curves were recalculated by averaging, for each data point, over 500 realizations of the perturbed hexagonal lattice and over 100 of the perturbed square lattice, with system sizes of roughly 2000 vertices, in order to ensure sufficient precision for the position of these lines in the case of periodic boundary conditions. We noticed non-negligible finite-

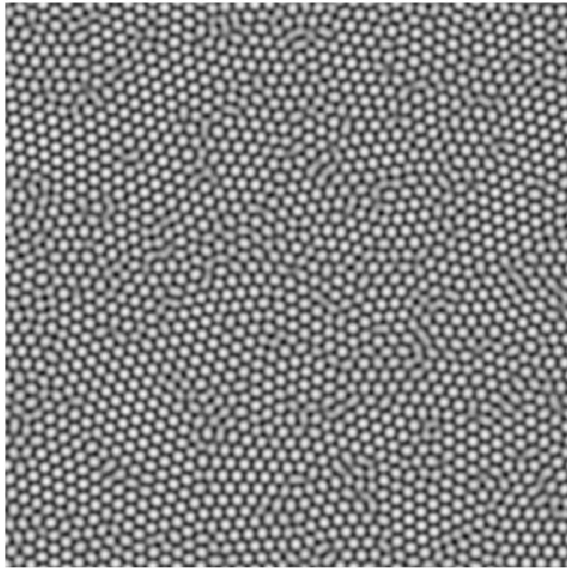


FIG. 10. Interface of the crystal from Fig. 1 (i.e.,  $\bar{G}=0.6$ ) at  $t=100.0$ .

size effects, so we made the randomly perturbed lattices equal in size to the simulated solidification structures.

We see from Fig. 13 that the simulated pattern moves, in the course of time, from a position off the upper dashed line towards it. While  $m$  keeps increasing, albeit more and more slowly, the standard deviation finally settles down to a value that does not seem to decrease anymore. This is most likely due to the remaining dynamic grain boundaries the system has difficulties getting rid of.

A comparison with the dynamical evolution of *experimental patterns* in the  $m\sigma$  diagram reveals similarities and differences (see Fig. 15). As in our simulation, the representative point of a system moves towards the line of perturbed hexagonal order. However, it approaches that line from above rather than from below, which is an indication that

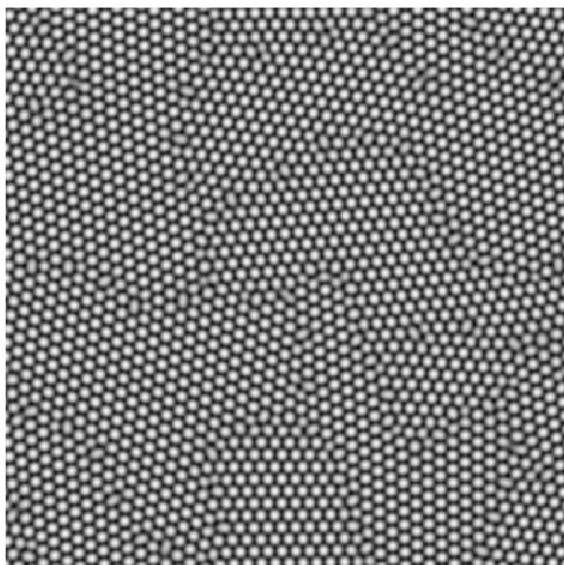


FIG. 11. Interface of the crystal from Fig. 1 (i.e.,  $\bar{G}=0.6$ ) at  $t=3300.0$ .

$\bar{G} = 0.6, t = 3300.0$

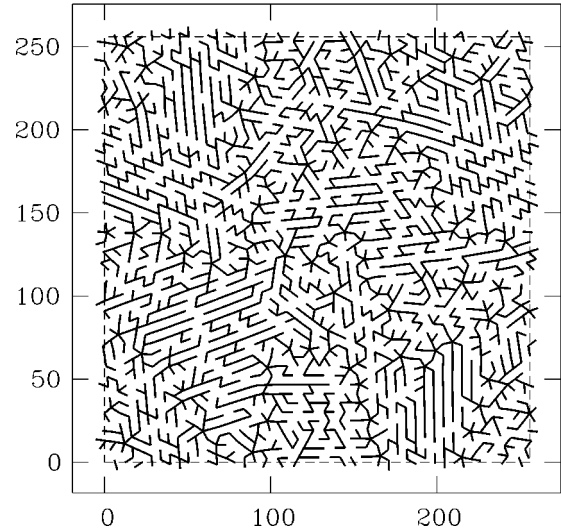


FIG. 12. Minimum spanning tree for  $t=3300.0$  ( $\bar{G}=0.6$ ).

random initial conditions miss some aspects of the experimental initial state. It appears that they lead to a too narrow cell size distribution. Experimental distributions seem to contain a larger percentage of very big and very small cells initially (this is vindicated by Fig. 2).

Moreover, our structures are generally more ordered than the experimental ones:  $m$  is larger than in the experimental patterns. This is due to our using the symmetric model in which the birth and death of cells and cell rearrangement are easier than in the experiment, where diffusion in the solid is essentially absent. Nevertheless, there remains an effective trapping of dynamic grain boundaries even in the symmetric model. We have verified that it is not simply due to the fact that we use a square lattice on which no undistorted hexagonal structures are possible for we observe the same imperfect structures and long-time trapping of grain boundaries in simulations on a hexagonal grid in a hexagonal geometry.

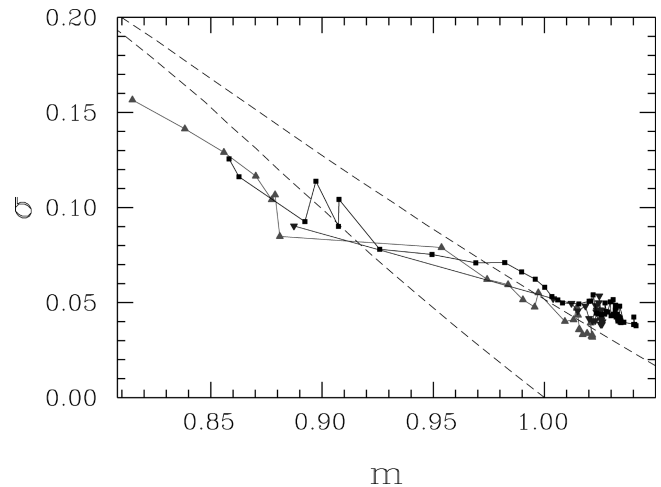


FIG. 13. Dynamics in the  $m\sigma$  plane of the representative point of the system shown in Figs. 1, 10, and 11 ( $\bar{G}=0.6$ ) and two other systems ( $\bar{G}=0.5$  and  $\bar{G}=0.4$ ). Time varies between  $t=2.5$  and 30 000 for  $\bar{G}=0.6$ ,  $t=10$  and 10 000 for  $\bar{G}=0.5$ , and  $t=1$  and 6000 for  $\bar{G}=0.4$ .

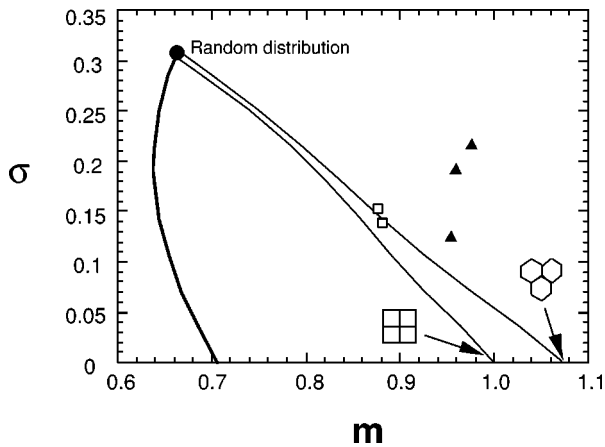


FIG. 14.  $m\sigma$  plot of some ideal lattices and some experimental systems.

Comparable results are obtained when we decrease the temperature gradient to  $\bar{G}=0.5$ , the main difference being a higher degree of disorder, resulting in a larger overall number of defects (but see Sec. IV C). On further decreasing the temperature gradient to  $\bar{G}=0.4$ , we observe similar behavior initially. However, the system does not indefinitely evolve towards a state of increasing apparent order. Instead, the shape of the cluster number function starts to become rounded and thinner again after an initial ordering process, as becomes clear from Fig. 16. This is a signature of the appearance, in each instantaneous picture of the interface, of several types of cells, larger ones and smaller ones. Figure 17 exemplifies this, and the reader will easily be convinced that the differentiation into cells with different heights must lead to such a change in the shape of the cluster number function. An investigation of the *dynamics* of the pattern of Fig. 17 shows that it is *oscillatory*. This is directly seen in an animation of a sequence of interfaces, which unfortunately cannot be given in this medium. However, closer inspection of the

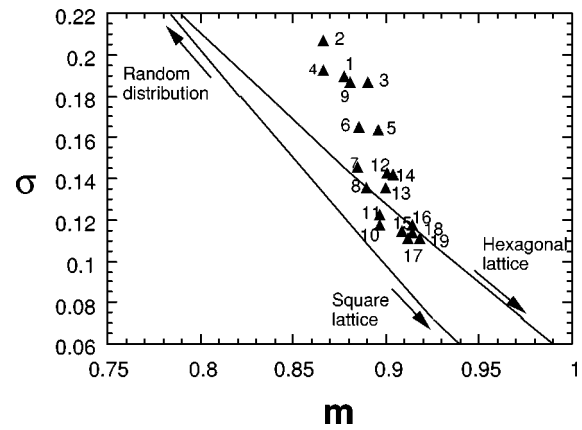


FIG. 15. Temporal evolution of the representative point of the system succinonitrile 0.5 % wt. acetone ( $V=2.1 \mu\text{m/s}$ ) in the  $m\sigma$  plot. The numbers near the triangles indicate the temporal sequence of the experimental structures.

figure reveals that in most grains of the pattern [the grain structure is depicted in Fig. 17(b)] a cell has a size different from that of its six neighbors and the sizes of those are alternating. These three different sizes correspond to different phases of the oscillation of each of the cells.

In the  $m\sigma$  plane, the oscillations lead to the representative point of the system approaching a fixed point near the line of perturbed hexagonal structures and making small excursions about it (Fig. 13). The pattern oscillates but still has a strong random component; cells that are far from each other oscillate out of phase.

The large scale of our simulations prevents our making very precise statements about the position of the bifurcation from a stationary to an oscillatory state. To be able to run our largest systems for long times, we had to choose a relatively big lattice constant,  $h=0.5$ . On reduction of this to  $h=0.4$ , oscillatory patterns seem to appear only at values below  $\bar{G}=0.4$  but above 0.35. For one-dimensional interfaces, we

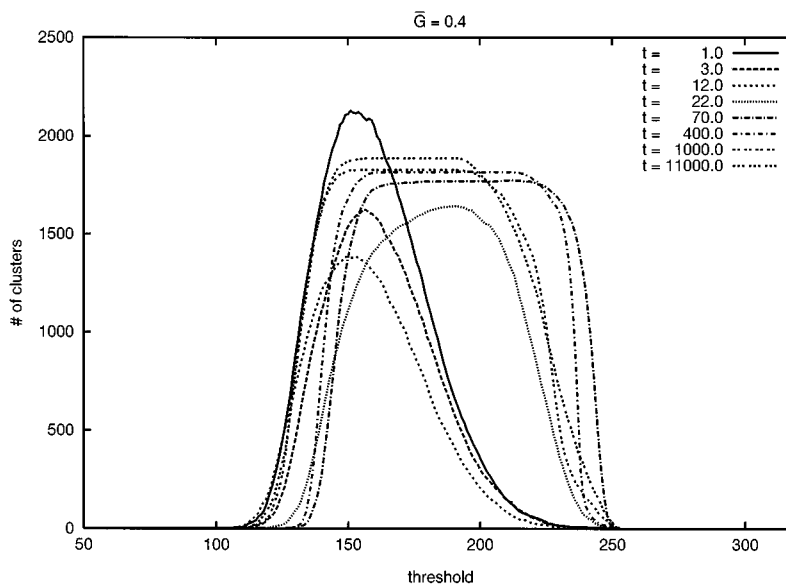
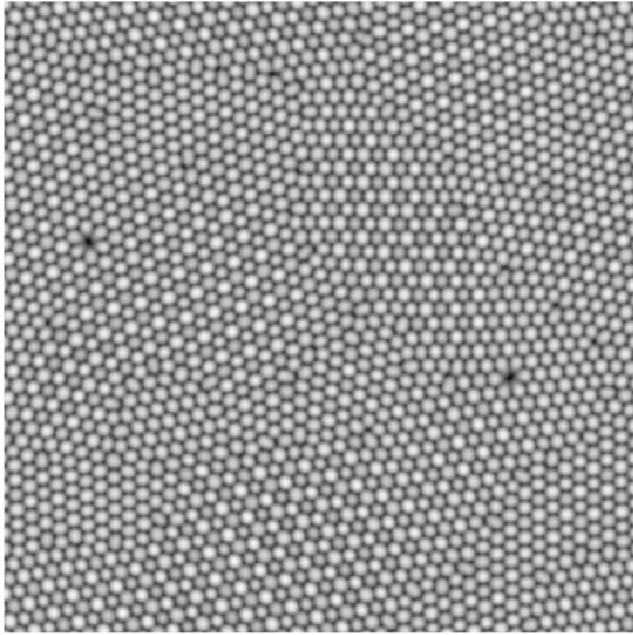
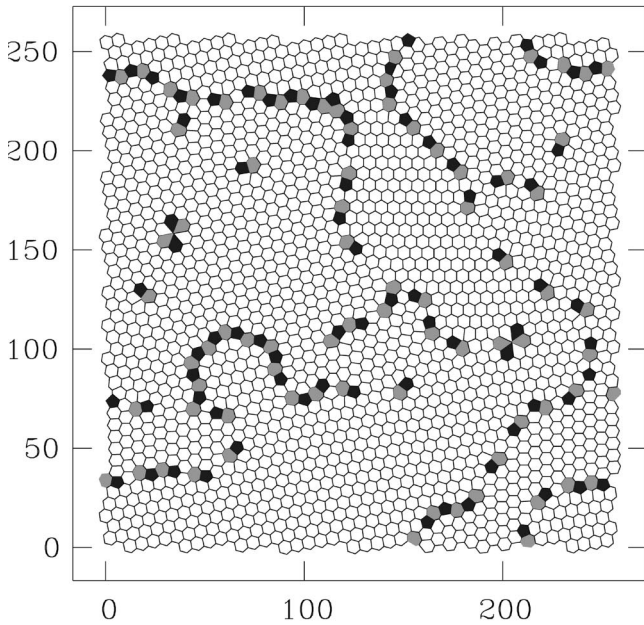


FIG. 16. Dynamics of the cluster number function for  $\bar{G}=0.4$ .



(a)

$\bar{G} = 0.4, t = 11000.0$



(b)

FIG. 17. (a) Oscillatory interface in the case  $\bar{G}=0.4$  ( $t=11\,000$ ). (b) Corresponding defect structure.

know the bifurcation to arise at  $\bar{G} \approx 0.32$  [28]; for two-dimensional ones we expect it at a larger value of  $\bar{G}$  since it is due to an interaction between modes of wave numbers  $q$  and  $\sqrt{3}q$  rather than between modes of wave numbers  $q$  and  $2q$  as for one-dimensional interfaces [43].

The basic behavior of these oscillatory structures has been studied in smaller systems and starting from regular initial

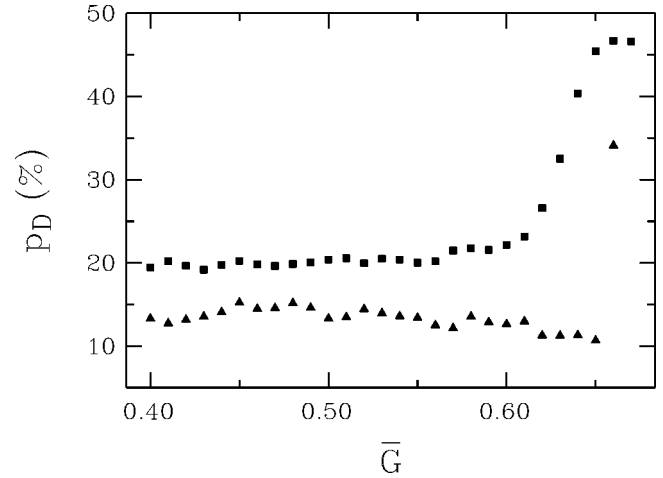


FIG. 18. Percentage of defects  $p_D$  as a function of  $\bar{G}$  at  $t=100$  (squares) and  $t=500$  (triangles). For  $\bar{G}=0.67$ , the pattern starts out developing cells, visible at  $t=100$ , but then tends to the planar interface, so there are no data for  $t=500$ . The system size is  $256 \times 256$ .

states in Ref. [43]. It turns out that the generic oscillatory mode consists in three neighboring cells oscillating at phase shifts of  $\pm 2\pi/3$  with respect to each other. This leads to a spatial period tripling of the basic pattern. Our discovery here is that this oscillatory structure appears *spontaneously* in *extended* systems and thus must be stable. In small systems, we have been able to produce oscillatory patterns with a phase shift of  $\pi$  between one half of the cells and the other. These patterns also have tripled periodicity with respect to the basic state. However, they did not appear in our extended-system simulations, so they are probably not stable. Moreover, we have so far seen no signature of regular *drifting* patterns [43] in an extended system, suggesting that these patterns are, as in two-dimensional systems [28], unstable with respect to phase diffusion. On the other hand, drifting patterns with frozen-in defects are possible (see below).

### C. Late-stage growth

The simplest measure of disorder associable with defects is the fraction of the total pattern consisting of defects, regardless of their nature, i.e., of whether they correspond to triangles, quadrangles, pentagons, heptagons, or polygons with more edges. Therefore, we simply count the cells and determine their nonhexagonal fraction. Invariably, at later stages of growth ( $t > 1000$ ), when the order of the pattern increased, these defects consisted almost exclusively of equal numbers of pentagons and heptagons, so the percentages that are given below correspond to twice the percentage of pentagons and heptagons, respectively. Also, at these times the variation of the total number of cells is well below the percent range, so defect fractions are a good measure for absolute defect numbers too.

An interesting quantity is the percentage  $p_D$  of defects as a function of  $\bar{G}$  for a fixed time. We expected this to be a decreasing function of  $\bar{G}$ . A simulation for twenty-six  $\bar{G}$  values between 0.4 and 0.65 in large systems (size  $256 \times 256$ ) revealed, however, as is exhibited in Fig. 18, that

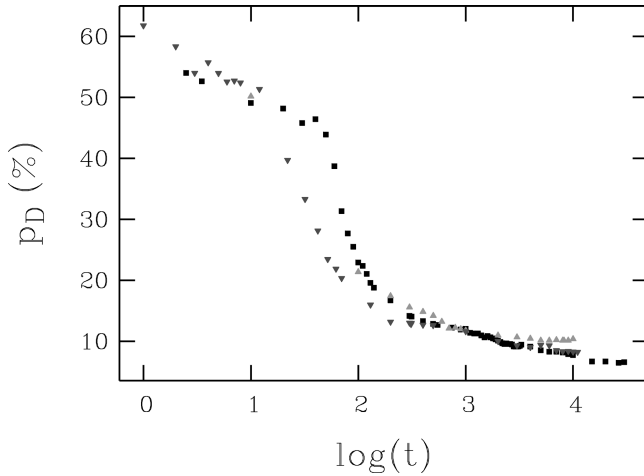


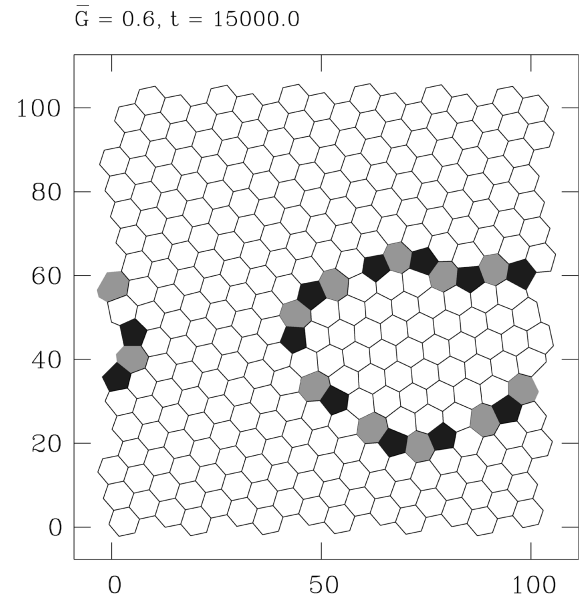
FIG. 19. Percentage of defects as a function of time for  $\bar{G}=0.6$  (squares),  $\bar{G}=0.5$  (upward triangles), and  $\bar{G}=0.4$  (downward triangles), at a system size of  $256 \times 256$ . Logarithms are with respect to the base 10.

at time  $t=100$  the number of defects *increases* as  $\bar{G}=\bar{G}_c$  is approached. This tendency reverses itself towards the expected trend when  $t$  is increased to 500. The first explanation that comes to mind, namely, the slowing down of the instability near threshold, can hardly be correct. A look at *earlier* times than  $t=100$ , for which we have data from the runs for  $\bar{G}=0.4, 0.5$ , and  $0.6$ , clearly shows that there the order is as expected, i.e., highest percentage of defects at  $\bar{G}=0.4$ , lowest at  $\bar{G}=0.6$ . (The point at  $\bar{G}=0.66$  in the figure probably *does* exhibit slowing down since it moves towards smaller defect numbers much more slowly than the points with lower  $\bar{G}$ .)

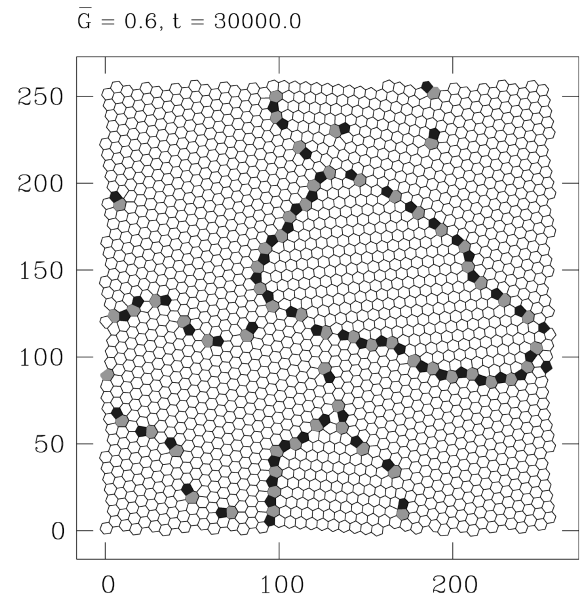
Currently, we do not have a good explanation for defect numbers increasing with  $\bar{G}$ . Since this happens in a temporal range that is interesting in experiments, it may, however, render a systematic classification of patterns according to their degree of defect disorder quite problematic.

Displaying the number of defects as a function of time for our longer simulations of large systems, we notice that there are again three distinct phases (Fig. 19): an initial stage, corresponding to the early dynamics discussed in Sec. IV A, during which the defect number drops steadily; an intermediate phase, in which it drops much more strongly as the cells equalize; and a late stage, when defect dynamics becomes much slower. During this last time range the number of defects decreases roughly proportional to  $\log_{10}t$ . However, the slope in our plot of  $p_D$  versus  $\log_{10}t$  seems to decrease further, so the time dependence of the approach to a perfect structure needs further discussion.

Because these systems are too large to follow the dynamics until all defects may have vanished, we have simulated smaller systems, in order to check whether they will become completely ordered eventually. Since in our largest systems ( $256 \times 256$ ), grain sizes typically approach a quarter of the total system size, we considered systems with a size of  $62.5 \times 62.5$  and  $\bar{G}$  values between 0.4 and 0.65. In these systems, all defects disappeared within the maximum consid-



(a)



(b)

FIG. 20. Pattern of defect lines for  $\bar{G}=0.6$  for (a) system size  $102.4 \times 102.4$  and  $t=10\,000$  and (b) system size  $256 \times 256$  and  $t=30\,000$ .

ered time span,  $t=10\,000$ , whenever  $\bar{G}$  was larger than or equal to 0.6. Increasing the system size to  $102.4 \times 102.4$  and  $128 \times 128$ , respectively, we find that the system with  $\bar{G}=0.6$  will end up perfectly ordered by  $t=10\,000$  in some cases and keep on the order of 3% defects in others, depending on initial conditions.

Thus our simulations seem to suggest that close enough to threshold any system will tend to perfect hexagonal order in the long run. Therefore, crystal surfaces in directional solidification are definitely not candidates for the appearance of turbulent interfaces *at the instability threshold*, a theoretical

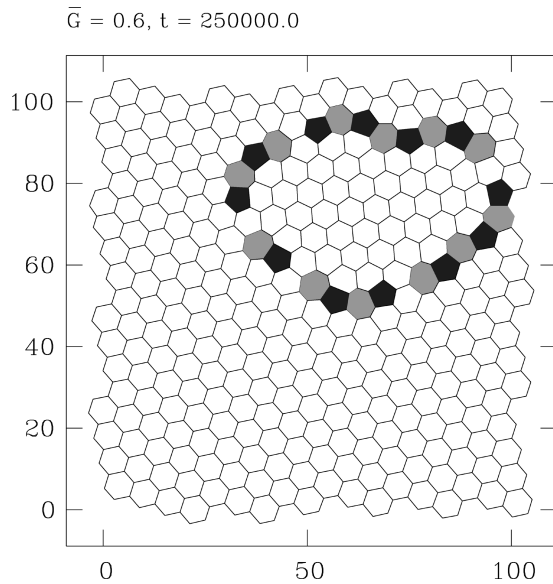


FIG. 21. Same system as in Fig. 20(a), but at  $t = 250\,000$ .

scenario suggested by Newell and Pomeau [53].

As  $\bar{G}$  is decreased, the number of defects remaining after a sufficient time lapse first increases but decreases again with the appearance of oscillatory patterns. This can be seen in Fig. 19, where at late times the number of defects is smaller in the system with  $\bar{G} = 0.4$  than in that with  $\bar{G} = 0.5$  (but larger than for  $\bar{G} = 0.6$ ). Thus oscillations give the system additional flexibility to reduce the number of defects.

It is interesting to consider the pattern of defect lines in the most ordered systems that we have investigated systematically. Figure 20 shows two examples at  $\bar{G} = 0.6$ . Apparently, the defects have a tendency to form ringlike structures, suggesting a simplified description of the late-time dynamics to be possible in terms of defect lines, using concepts such as a line energy conveying a tendency to the defect lines to shorten via the annihilation of pairs of defects. This shortening process is accompanied by local rotation of small domains of cells but not of whole grains, which we find to keep their orientation. In an infinite system, perfect alignment may be achieved, meaning that in the long run, one orientation will survive at the expense of all others.

In finite systems, at least, defects can survive indefinitely. With very small systems (containing some 25 cells), we have found pointlike defect patterns to persist in a stationary configuration. In the intermediate-size system of Fig. 20, we have continued the temporal evolution up to  $t = 250\,000$  and we find the ring of defects to be stable and to *propagate* very slowly upward and to the left, which is shown in Fig. 21. It appears that a single asymmetric ring of defects has some of the characteristics of a *solitary wave* in two dimensions. These patterns call for attempts at an experimental realization.

Thus the existence of a fourth stage of the dynamics seems likely, starting when all surviving grains have the shortest boundaries compatible with their area. Then a decrease in the local misalignment of cells will no longer suffice to reduce the length of defect lines. To proceed towards order grains must either shrink or flip their orientation as a

whole, both processes that we expect to be extremely slow. Alternatively, they might survive forever, meaning that the picture of line energies would be too crude to capture the actual nonequilibrium dynamics of the system.

Finally, it should be mentioned that in a system with  $\bar{G} = 0.35$ , we observed the number of defects to pass through a minimum in the course of time. It increased strongly at later times, which we take as an indication for the system becoming turbulent. We will not go into details here.

## V. CONCLUSIONS

To summarize, we have studied theoretically, by way of numerical solution of a simplified local interface equation, the temporal evolution of cell arrays in directional solidification. We have performed a number of simulations for times that exceed experimentally accessible periods, at least in the low-velocity limit, and for a variety of system sizes and parameters. The important theoretical parameter is a renormalized temperature gradient, varied from the threshold of the primary Mullins-Sekerka instability to the onset of chaotic solutions.

Our main findings are the following. There are (at least) three stages of growth. In the first, a local selection process determines the basic length scale of the pattern. This scale is not far from the fastest-growing mode of linear stability theory.

In the second stage, lasting a few hundred diffusion times (hours to days in experiments), the cells become more similar to each other and the pattern orders in the form of dynamical “crystalline” grains. This is the stage of the fastest decay of defects. If the pattern is far enough from threshold, it will become oscillatory and topologically *more* ordered.

The final stage (accessible to our numerics) is a slow process of defect elimination by local reorientation of grain parts and migration of defect lines. Close enough to threshold, the system may become completely ordered, which for large enough systems will probably occur through a fourth, even slower, stage of grain elimination. For oscillatory systems, complete *topological* order is also a possibility (although we have not seen examples for this), even when the *metric* disorder remains, associated with the standard deviation of the edge length distribution in the minimum spanning tree.

Whether there is a region of  $\bar{G}$  values above the domain of oscillatory patterns and below the ordered ones, where a certain percentage of defects must persist in the pattern, is an interesting open question. The answer may also depend on the boundary conditions of the system, i.e., while infinitely extended or large systems with periodic boundary conditions will order, systems confined to small unfavorable geometries may be forced to accommodate a certain number as defects, similar to observations in Bénard-Marangoni convection [51].

## ACKNOWLEDGMENTS

It is a pleasure to acknowledge stimulating discussions with C. Misbah and I. Daumont on similarities and differences between the dynamics of directional solidification and that of a stabilized Kuramoto-Sivashinsky equation.

- [1] B. Billia, H. Jamgotchian, and H. Nguyen Thi, in *Growth and Form*, edited by M. Ben Amar *et al.* (Plenum, New York, 1991).
- [2] Q. Li, H. Nguyen Thi, H. Jamgotchian, and B. Billia, *Acta Metall. Mater.* **43**, 1271 (1995).
- [3] P. Oswald, J. Bechhoefer, A. Libchaber, and F. Lequeux, *Phys. Rev. A* **36**, 5832 (1987).
- [4] A. J. Simon, J. Bechhoefer, and A. Libchaber, *Phys. Rev. Lett.* **63**, 2574 (1989).
- [5] R. Trivedi and K. Somboonsuk, *Acta Metall.* **33**, 1061 (1985).
- [6] S. de Cheveigné, C. Guthmann, and M. M. Lebrun, *J. Phys. (France)* **47**, 2095 (1986).
- [7] S. de Cheveigné, C. Guthmann, P. Kurowski, E. Vicente, and H. Biloni, *J. Cryst. Growth* **92**, 616 (1988).
- [8] P. Kurowski, C. Guthmann, and S. de Cheveigné, *Phys. Rev. A* **42**, 7368 (1990).
- [9] S. de Cheveigné and C. Guthmann, *J. Phys. I* **2**, 193 (1992).
- [10] B. Caroli, C. Caroli, and B. Roulet, *J. Phys. (France)* **43**, 1767 (1982).
- [11] D. J. Wollkind, D. B. Oulton, and R. Sriranganathan, *J. Phys. (France)* **45**, 505 (1984).
- [12] L. H. Ungar and R. A. Brown, *Phys. Rev. B* **29**, 1367 (1984).
- [13] L. H. Ungar and R. A. Brown, *Phys. Rev. B* **30**, 3993 (1984).
- [14] L. H. Ungar, M. J. Bennett, and R. A. Brown, *Phys. Rev. B* **31**, 5923 (1985).
- [15] L. H. Ungar and R. A. Brown, *Phys. Rev. B* **31**, 5931 (1985).
- [16] P. Pelcé and Y. Pomeau, *Stud. Appl. Math.* **74**, 245 (1986).
- [17] T. Dombre and V. Hakim, *Phys. Rev. A* **36**, 2811 (1987).
- [18] M. B. Amar and B. Moussallam, *Phys. Rev. Lett.* **60**, 317 (1988).
- [19] Y. Saito, C. Misbah, and H. Müller-Krumbhaar, *Phys. Rev. Lett.* **63**, 2377 (1989).
- [20] D. A. Kessler and H. Levine, *Phys. Rev. A* **39**, 3041 (1989).
- [21] K. Brattkus and C. Misbah, *Phys. Rev. Lett.* **64**, 1935 (1990).
- [22] H. Levine and W. Rappel, *Phys. Rev. A* **42**, 7475 (1990).
- [23] C. Misbah, H. Müller-Krumbhaar, and Y. Saito, *J. Cryst. Growth* **99**, 156 (1990).
- [24] A. Classen, C. Misbah, H. Müller-Krumbhaar, and Y. Saito, *Phys. Rev. A* **43**, 6920 (1991).
- [25] K. Kassner, C. Misbah, and H. Müller-Krumbhaar, *Phys. Rev. Lett.* **67**, 1551 (1991).
- [26] A. Valance, K. Kassner, and C. Misbah, *Phys. Rev. Lett.* **69**, 1544 (1992).
- [27] W.-J. Rappel and H. Riecke, *Phys. Rev. A* **45**, 846 (1992).
- [28] K. Kassner, C. Misbah, H. Müller-Krumbhaar, and A. Valance, *Phys. Rev. E* **49**, 5477 (1994); **49**, 5495 (1994).
- [29] H. Nguyen Thi, B. Billia, and H. Jamgotchian, *J. Fluid Mech.* **205**, 581 (1989).
- [30] H. Nguyen Thi, B. Billia, and L. Capella, *J. Phys. (France)* **51**, 625 (1990).
- [31] N. Noël, thèse de doctorat, Université d'Aix-Marseille III, 1996 (unpublished); N. Noël, H. Jamgotchian, and B. Billia, *J. Cryst. Growth* **181**, 117 (1997).
- [32] Note that whenever the description of the system may be restricted to that of the interface alone, a two-dimensional system may be described by equations for a one-dimensional interface and a three-dimensional one by equations for a two-dimensional interface. In the following, when we talk about the system, we mean the bulk, i.e., a three- or two-dimensional object, whereas when talking about the interface, we will refer to the two- or one-dimensional case, respectively.
- [33] Y. Saito, G. Goldbeck-Wood, and H. Müller-Krumbhaar, *Phys. Rev. Lett.* **58**, 1541 (1987).
- [34] K. Kassner, in *Informatik-Fachberichte*, edited by D. Krönig and M. Lang (Springer, Berlin, 1992), Vol. 306, p. 259.
- [35] A. A. Wheeler, B. T. Murray, and R. J. Schaefer, *Physica D* **66**, 243 (1993).
- [36] R. Kobayashi, *Exp. Math.* **3**, 59 (1994).
- [37] A. Karma and W.-J. Rappel, *Phys. Rev. Lett.* **77**, 4050 (1996).
- [38] T. Abel, E. Brener, and H. Müller-Krumbhaar, *Phys. Rev. E* **55**, 7789 (1997).
- [39] B. Grossmann, K. R. Elder, M. Grant, and J. M. Kosterlitz, *Phys. Rev. Lett.* **71**, 3323 (1993).
- [40] K. Brattkus and S. H. Davis, *Phys. Rev. B* **38**, 11 452 (1988).
- [41] A. Ghazali and C. Misbah, *Phys. Rev. A* **46**, 5026 (1992).
- [42] C. Misbah and A. Valance, *Phys. Rev. E* **49**, 166 (1994).
- [43] I. Daumont, K. Kassner, C. Misbah, and A. Valance, *Phys. Rev. E* **55**, 6902 (1997).
- [44] A possible exception, in the case of one-dimensional interfaces, is one instability that is present in the more generic KS equation [42] but apparently absent in directional solidification.
- [45] B. Billia, H. Jamgotchian, and H. Nguyen Thi, *Metall. Trans. A* **22**, 3041 (1991).
- [46] The diffusion time is given by  $\tau = D/V^2$  and a numerical value for a typical experiment would be  $\tau = 1000$  s ( $D = 10^{-5}$  cm<sup>2</sup>/s and  $V = 1$   $\mu$ m/s).
- [47] K. R. Mecke, *Phys. Rev. E* **53**, 4794 (1996).
- [48] J. Serra, *Image Analysis and Mathematical Morphology* (Academic, New York, 1982).
- [49] L. A. Santaló, *Integral Geometry and Geometric Probability* (Addison-Wesley, Reading, MA, 1976).
- [50] C. Dussert, G. Rasigni, M. Rasigni, J. P. Palmari, and A. Leebaria, *Phys. Rev. B* **34**, 3528 (1986).
- [51] P. Cerisier, R. Ocelli, C. Pérez-García, and C. Jamond, *J. Phys. (France)* **48**, 569 (1987); P. Cerisier, S. Rahal, and B. Billia, *Phys. Rev. E* **54**, 3508 (1996).
- [52] K. D. Pithia and S. F. Edwards, *Physica A* **215**, 277 (1995).
- [53] A. Newell and Y. Pomeau, *J. Phys. A* **36**, L429 (1993).